

The case for electron re-acceleration at galaxy cluster shocks

Reinout J. van Weeren^{1*}, Felipe Andrade-Santos¹, William A. Dawson², Nathan Golovich³, Dharam V. Lal⁴, Hyesung Kang⁵, Dongsu Ryu^{6,7}, Marcus Brüggen⁸, Georgiana A. Ogrean⁹, William R. Forman¹, Christine Jones¹, Vinicius M. Placco¹⁰, Rafael M. Santucci¹¹, David Wittman^{3,12}, M. James Jee¹³, Ralph P. Kraft¹, David Sobral^{14,15}, Andra Stroe¹⁶ and Kevin Fogarty¹⁷

On the largest scales, the Universe consists of voids and filaments making up the cosmic web. Galaxy clusters are located at the knots in this web, at the intersection of filaments. Clusters grow through accretion from these large-scale filaments and by mergers with other clusters and groups. In a growing number of galaxy clusters, elongated Mpc-sized radio sources have been found^{1,2}. Also known as radio relics, these regions of diffuse radio emission are thought to trace relativistic electrons in the intracluster plasma accelerated by low-Mach-number shocks generated by cluster-cluster merger events³. A long-standing problem is how low-Mach-number shocks can accelerate electrons so efficiently to explain the observed radio relics. Here, we report the discovery of a direct connection between a radio relic and a radio galaxy in the merging galaxy cluster Abell 3411-3412 by combining radio, X-ray and optical observations. This discovery indicates that fossil relativistic electrons from active galactic nuclei are re-accelerated at cluster shocks. It also implies that radio galaxies play an important role in governing the non-thermal component of the intracluster medium in merging clusters.

Cluster mergers are the most energetic events in the Universe after the Big Bang, releasing energies up to $\sim 10^{64}$ erg on Gyr timescales. Most of the gravitational energy released during cluster merger events is converted into thermal energy via low-Mach-number shocks ($M \lesssim 3$) and turbulence in the intracluster medium (ICM)⁴. A small fraction ($<1\%$, approximately) of the energy dissipated at shocks could be channeled into the acceleration of cosmic rays (CR). In the presence of magnetic fields, CR electrons would then emit synchrotron radiation, which can be observed with radio telescopes. The origin of the large-scale magnetic fields, and the nature of particle acceleration processes that operate in these dilute cosmic plasmas, are still open questions.

The ICM has a high thermal-to-magnetic pressure ratio, β , and electron acceleration by low-Mach-number collisionless shocks in

such high- β plasmas is poorly understood, as analytical calculations cannot properly capture the non-linear behavior of this process⁵. Radio relics, elongated sources that trace the CR at ICM shocks, provide us with rare opportunities to probe this process. While there is substantial evidence that relics trace CR electrons at shocks^{6,7}, previous work has found that the acceleration efficiency should be very low at these shocks, if these synchrotron emitting electrons are accelerated from the thermal pool of the ICM via the diffusive shock acceleration (DSA) mechanism⁵. This low efficiency is hard to reconcile with the observed brightness of some radio relics, suggesting a high acceleration efficiency⁸⁻¹⁰. In addition, some relics have regions with rather flat radio spectra ($\alpha \approx -0.7$; $F_\nu \propto \nu^\alpha$, where α is the spectral index, F_ν the flux density, and ν the frequency), but the corresponding Mach numbers for the shocks, as measured via X-ray observations, are low^{11,12}. This contradicts predictions based on the DSA mechanism¹³. This long-standing problem has so far remained unsolved. Furthermore, large merger shocks have been found without corresponding radio relics¹⁴, indicating that our understanding of particle acceleration by low-Mach-number shocks is still incomplete.

Recently, new insights into the phenomenon have been obtained from particle-in-cell (PIC) simulations¹⁵. These PIC simulations show that acceleration from the thermal pool may be possible. However, for some relics, an unrealistic fraction of the shock energy needs to be transferred into the non-thermal electron population to explain their radio brightness^{12,16,17} and the PIC simulations do not solve this problem. A solution to explain the apparently very efficient acceleration is to invoke the presence of a population of fossil relativistic electrons¹⁸, with Lorentz factors (γ) greater than $\sim 10^2$. The synchrotron lifetime of relativistic electrons in the ICM is relatively short ($\sim 10^8$ yr). Once these electrons have lost most of their energy, they do not radiate within the observable radio band and thereby become invisible to radio telescopes. It has been suggested that these fossil electrons, which have Gyr lifetimes, can be efficiently re-accelerated at shocks and are therefore able to create bright radio relics^{9,19}.

¹Harvard-Smithsonian Center for Astrophysics, 60 Garden Street, Cambridge, Massachusetts 02138, USA. ²Lawrence Livermore National Laboratory, 7000 East Avenue, Livermore, California 94550, USA. ³University of California, 1 Shields Avenue, Davis, California 95616, USA. ⁴National Centre for Radio Astrophysics, TIFR, Pune University Campus, Post Bag 3, Pune 411007, India. ⁵Department of Earth Sciences, Pusan National University, Busan 46241, Korea. ⁶Department of Physics, UNIST, Ulsan 44919, Korea. ⁷Korea Astronomy and Space Science Institute, Daejeon 34055, Korea. ⁸Hamburger Sternwarte, Hamburg University, Gojenbergsweg 112, 21029 Hamburg, Germany. ⁹Kavli Institute for Particle Astrophysics and Cosmology, Stanford University, 452 Lomita Mall, Stanford, California 94305-4085, USA. ¹⁰Department of Physics and JINA Center for the Evolution of the Elements, University of Notre Dame, Notre Dame, Illinois 46556, USA. ¹¹Departamento de Astronomia - Instituto de Astronomia, Geofísica e Ciências Atmosféricas, Universidade de São Paulo, São Paulo, SP 05508-900, Brazil. ¹²Instituto de Astrofísica e Ciências do Espaço, Universidade de Lisboa, Lisbon 1749-016, Portugal. ¹³Department of Astronomy and Center for Galaxy Evolution Research, Yonsei University, 50 Yonsei-ro, Seoul 03722, Korea. ¹⁴Department of Physics, Lancaster University, Lancaster LA1 4YB, UK. ¹⁵Leiden Observatory, Leiden University, PO Box 9513, NL-2300 RA Leiden, the Netherlands. ¹⁶European Southern Observatory, Karl-Schwarzschild-Straße 2, D-85748 Garching bei München, Germany. ¹⁷Department of Physics and Astronomy, Johns Hopkins University, 3400 North Charles Street, Baltimore, Maryland 21218-2686, USA. *e-mail: rvanweeren@cfa.harvard.edu

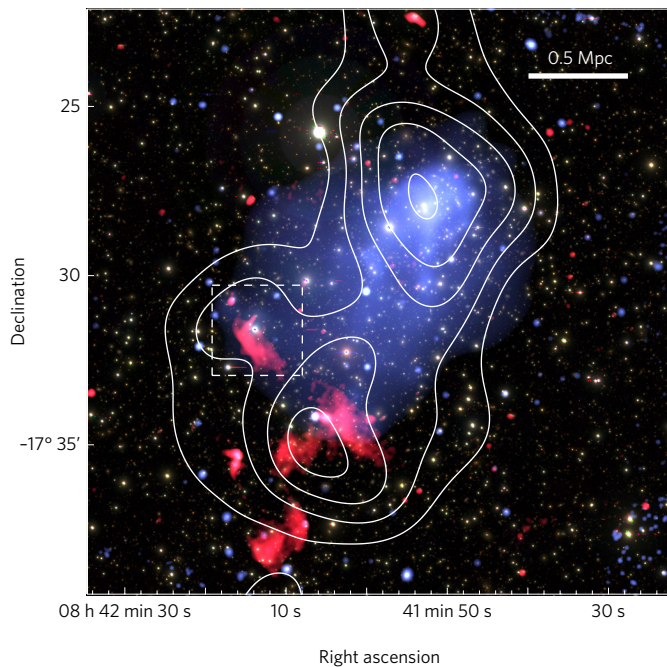


Figure 1 | Subaru gri colour image of the merging cluster Abell 3411–3412. Radio emission at 610 MHz from the GMRT is shown in red. The 0.5–2.0 keV Chandra X-ray image is shown in blue. The galaxy distribution is shown with white contours. Contour levels are drawn at (3, 4, 5,...) galaxies arcmin⁻². The dashed box indicates the region shown in Fig. 3.

Obvious candidates for such fossil electrons are the (old) lobes and tails of radio galaxies^{7,20,21}. This fossil radio plasma can occupy a significant volume of the ICM due to turbulent diffusion, aided by the galaxy motions throughout the ICM and the ICM motion itself. Indeed, some observational evidence to support this model has been reported. The complex morphologies of some radio relics resemble those of disturbed tailed radio galaxies that are often found in merging galaxy clusters^{7,20}. Two prime examples are the relics in the Bullet and PLCKG287.0 + 32.9 clusters^{7,22}. However, in the case of PLCKG287.0 + 32.9, no redshift for the putative radio galaxy connected to the relic could be obtained, since the proposed core of the radio galaxy did not have an optical counterpart²⁰. Similarly, no direct link between the relic in the Bullet cluster and a tailed radio galaxy could be established⁷. The relic in the Coma cluster provides another interesting case. Here, a confirmed cluster radio galaxy seems to be connected to a relic²¹. Adiabatic compression of fossil plasma by a shock was proposed as a model for its origin^{23,24}. While the electrons do gain energy via the adiabatic compression, this model does not invoke any Fermi-type re-acceleration processes.

Here, we present optical, radio and X-ray observations of the merging galaxy cluster Abell 3411–3412 located at a redshift $z=0.162$. This cluster contains an Mpc-sized radio relic with an irregular shape^{25,26}. Chandra observations, totaling 211 ks, reveal a cluster with a cometary morphology undergoing a major merger event, with the compact core of one of the subclusters being the ‘head’ of the comet (Fig. 1). Our dynamical analysis, based on Keck spectra of 174 cluster members and Subaru imaging, indicates that this is an approximately 1:1 mass ratio merger viewed ~ 1 Gyr after core passage, with the merger axis being located close to the plane of the sky. The two subclusters are both very massive, with individual masses of $\sim 10^{15} M_{\odot}$. The core of the cluster coming in from the south (and currently observed in the north) was compact enough to survive the collision with the other cluster up to the present time, while the gas core of the subcluster that came in from the north was largely disrupted during the core passage.

Images at 610 and 325 MHz from the Giant Metrewave Radio Telescope (GMRT) show the large and complex radio relic located in the southern outskirts of the merging cluster (Fig. 2). Most interestingly, a close inspection of the northeastern component of the radio relic reveals an elongated narrow extension that leads from the relic towards a galaxy (source A, Figs 2 and 3a). This galaxy is a spectroscopically confirmed cluster member ($z=0.164$). A high-resolution 3 GHz Very Large Array (VLA) image shows an active galactic nucleus (AGN; radio core) at the galaxy’s centre. From the core, a narrow tail ‘feeds’ into the radio relic located ~ 90 kpc to its south. This reveals a direct connection between the relativistic plasma of an AGN and that of a radio relic. The probability of a chance projection of a tailed radio galaxy with this relic is 0.4%.

Our spectral index measurements between 0.325 and 3.0 GHz show that the radio spectrum steepens with distance from the compact nucleus from $\alpha=-0.5 \pm 0.1$ to $\alpha=-1.3 \pm 0.1$ (1σ errors), as is expected for synchrotron and inverse Compton losses (Fig. 3b). Notably, where the radio plasma from the AGN connects to the radio relic, the spectrum flattens back to $\alpha=-0.9 \pm 0.1$. This flattening is evidence for the re-acceleration of electrons from the radio tail at a shock. Moreover, we find evidence for spectral steepening across the relic in the direction towards the cluster center. These gradients have routinely been found for other relics and they are explained by electron energy losses in the downstream region of an outward-travelling shock²⁷. We also find that the outer edge of the relic is polarized, with a maximum polarization fraction of 40%. The emission-weighted average polarization fraction is 13% (Fig. 3c). The relatively modest spectral flattening at the shock suggests that it is not very strong. Furthermore, the existence of a downstream spectral index gradient (see Fig. 3b) suggests that adiabatic compression of a lobe of fossil radio plasma cannot be the sole cause of the relic.

To search for the shock, we extracted a 0.5–2.0 keV Chandra surface brightness profile in a sector containing the relic and fitted the profile by assuming an underlying broken power-law density model. At large radii, the density profiles of galaxy clusters are typically described by single power laws. However, the profile across the northeast part of the relic steepens sharply near the relic’s outer edge and shows a significant departure from a single power law, indicating a deviation from hydrostatic equilibrium as expected for a shock (Fig. 4). From this profile we conclude that the shock must be rather weak, with a Mach number below 1.7. This upper limit should be considered an approximate estimate due to the idealized assumptions about the shock geometry and projection effects.

Our observations of (1) a direct connection between a radio galaxy and the relic, (2) spectral flattening at the location where the radio tail meets the relic, (3) the presence of an X-ray surface brightness discontinuity at the relic’s outer edge, and (4) a high polarization fraction at the location of the flattest spectral indices provide the best evidence to date that radio galaxies in clusters provide seed electrons that can be re-accelerated and revived by merger shocks. Re-acceleration (and also adiabatic compression) counteracts the problem of low acceleration efficiency from the thermal pool. In addition, it provides a natural explanation why some cluster merger shocks have no corresponding radio relics. Those cases may lack a sufficient supply of fossil radio plasma. Finally, re-acceleration also solves the problem of the relatively flat spectral indices observed from relics, which for DSA, requires shocks that have higher Mach numbers than those observed in X-rays^{11,12}.

A number of re-acceleration models have been proposed: in one of these, fossil relativistic electrons are re-accelerated by a DSA-like process^{18,28} in combination with adiabatic compression; whereas, in another, re-acceleration occurs in the downstream region of the shock via magneto-hydrodynamical turbulence²⁸. Future work is needed to

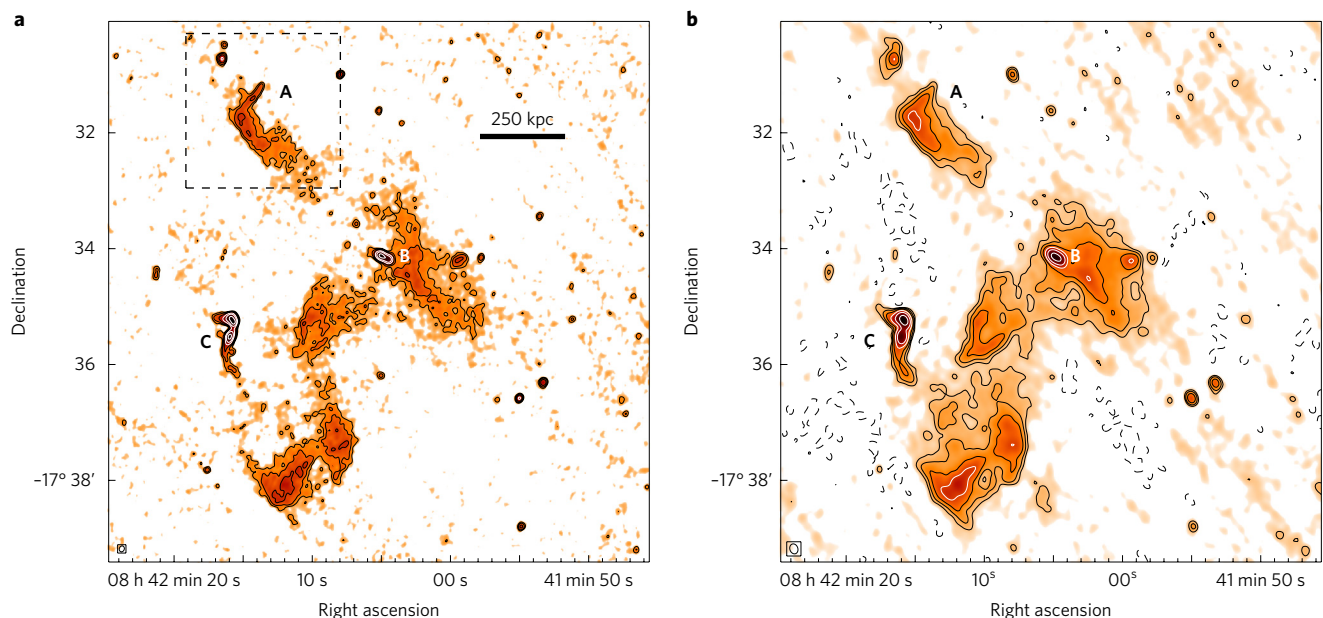


Figure 2 | GMRT radio images. **a**, GMRT 610 MHz image with contours drawn at levels of $\sqrt{(1,2,4,\dots)} \times 4 \sigma_{\text{rms}}$, where σ_{rms} is the map noise. The beam size is indicated in the bottom left corner. The dashed box indicates the region shown in Fig. 3. Cluster radio galaxies are labeled A, B and C. **b**, GMRT 325 MHz image. Contour levels are the same as those in **a**. Dotted contours are drawn at $-3 \sigma_{\text{rms}}$.

determine which of these re-acceleration mechanisms operates at radio relics²⁹, and whether re-acceleration is required to explain all relics. We evaluate one of these re-acceleration models in the Supplementary Information to investigate what Mach number is required to flatten the spectral index by the observed amount and examine the relatively uniform spectral index along the length of the shock front.

The Abell 3411–3412 cluster contains at least two additional radio galaxies about 2' to the south and 2' to southwest of the one described above (sources B and C; Fig. 2). One of the radio galaxies is embedded within the relic emission, and for the other, a tail of steep-spectrum radio emission extends towards the relic. Therefore, we think it is probable that the other components of the complex relic in Abell 3411–3412 also trace revived fossil plasma,

either by the process of adiabatic compression or by re-acceleration. Re-acceleration should also operate in other clusters because more examples of radio galaxies near relics have been found; for example, in the Coma Cluster²¹. Our results imply that PIC simulations and laboratory laser experiments³⁰ for collisionless shocks should include a relativistic fossil electron distribution in the upstream plasma. This study also indicates that to understand the non-thermal component of the ICM, the presence and distribution of radio galaxies needs to be taken into account, in addition to particle acceleration at shocks. Observations at low radio frequencies, particularly those obtained via LOFAR (the Low-Frequency Array), will be key to unveiling the connections between relics and AGNs, because low-frequency observations are sensitive to older, fossil radio plasma.

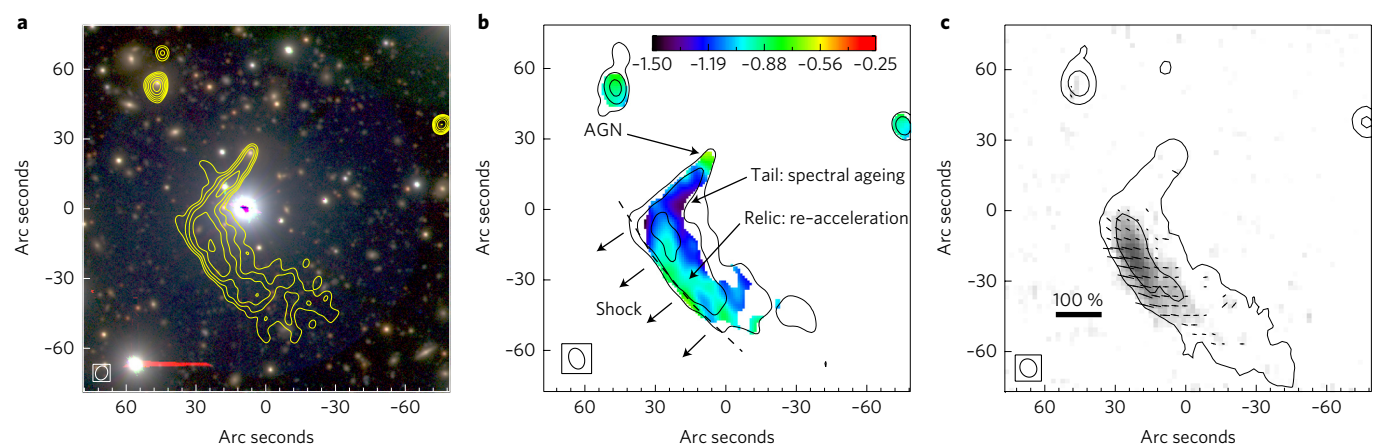


Figure 3 | Subaru optical, radio spectral index, and polarization maps of the northeast component of the radio relic in Abell 3411–3412. The beam sizes are indicated in the bottom left corner of the images. **a**, Subaru gri colour image. GMRT 610 MHz contours are overlaid in yellow. Contours are drawn at levels of $\sqrt{(1,2,4,\dots)} \times 5 \sigma_{\text{rms}}$. **b**, A spectral index map. The spectral index was determined using matched observations at frequencies of 0.325, 0.61, 1.5 and 3.0 GHz. Contours are from the 325 MHz GMRT image and are drawn at levels of $(1,2,4,\dots) \times 6 \sigma_{\text{rms}}$. The dashed line indicates the best-fitting position of the X-ray surface brightness edge. **c**, Polarization map at 3.0 GHz. Vectors display the electric field angles. The length of the vectors is proportional to the polarization fraction. A reference vector for 100% polarization is shown in the bottom left corner. The grayscale image shows the linear polarized intensity. Black contours trace the Stokes I continuum image and are drawn at (0.03, 0.12) mJy beam⁻¹.

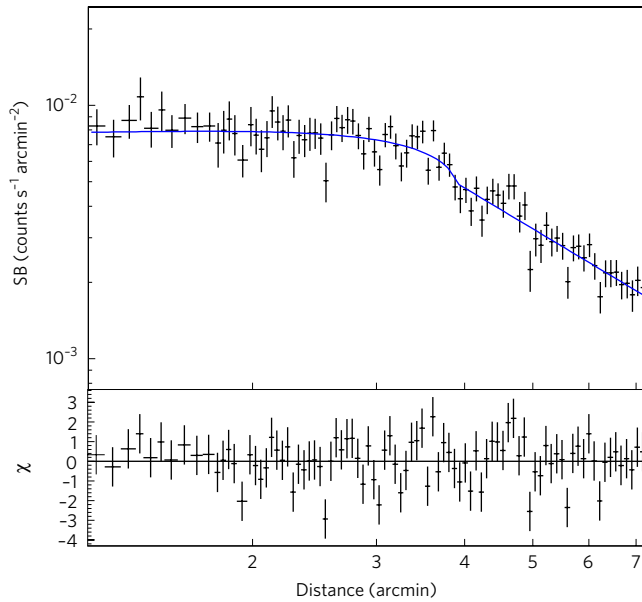


Figure 4 | Chandra 0.5–2.0 keV surface brightness (SB) profile across the radio relic in an elliptical sector (see the Supplementary Information). Uncertainties on the data points are plotted at the 1σ level. The blue line corresponds to the best-fitting density model. This double power-law model fits a jump (at a distance of $\sim 4'$) with a density compression factor $C = 1.31^{+0.10}_{-0.09}$. The position of this jump is indicated on the spectral index image (Fig. 3b).

Methods

Radio observations, data reduction and spectral indices. Abell 3411–3412 was observed with the GMRT on 21 October and 19 November 2012, at 610 and 325 MHz, respectively. A total bandwidth of 32 MHz was recorded. The on-source times were 4.5 h at 325 MHz and 3.6 h at 610 MHz. The initial calibration and visual removal of radio frequency interference (RFI) were carried out using the Astronomical Image Processing System (AIPS; <http://www.aips.nrao.edu/>). The initial calibration consisted of bandpass calibration, bootstrapping of the flux-density scale and the transfer of gains from the calibrator sources to the target field. The calibration solutions were further refined via the process of self-calibration using the CASA package³¹. For the imaging, W-projection was employed to account for the non-coplanar nature of the array^{32,33}. For the weighting, we employed the Briggs scheme with a robust parameter of 0.0, unless otherwise mentioned. The 610 MHz image has an rms noise (σ_{rms}) of $35 \mu\text{Jy beam}^{-1}$ and a resolution of $6.1'' \times 5.1''$. The 325 MHz image has a resolution of $10.5'' \times 8.3''$ and $\sigma_{\text{rms}} = 87 \mu\text{Jy beam}^{-1}$.

The cluster was also observed with the Karl G. Jansky VLA, covering the 2–4 GHz S-band in the B- and DnC-arrays on 26 February 2015 and 7 January 2016, respectively (project SG0455). The time on source was 1.2 h for both observing runs. In addition, 1–2 GHz L-band observations (project 15A-270) were obtained in BnA-array on 18 May 2015, with a total time on source of 0.5 h. These observations were reduced and calibrated with CASA following the process outlined in³⁴. RFI was automatically removed with the AOFlogger³⁵. The calibration consisted of delay, bandpass and gain corrections. The channel-dependent polarization leakage and angles were calibrated using the calibrators 3C147 and 3C138. The solutions were transferred to the target field and the solutions were further refined via the process of self-calibration. The imaging was carried out in the same way as for the GMRT data. For imaging of the L-band data, we also used 1.4 GHz VLA D-array observations (project AC0696) to include emission on larger scales that are missed by the B-array observations. The reduction and calibration of the D-array observations are described in²⁵. All images were corrected for primary beam attenuation.

To generate the spectral index maps, we acquired images at 0.325 and 3.0 GHz and uniform weighting was employed to correct for the different sampling densities in the u - v plane. We also added inner u - v -range cuts so that only common u - v -ranges were imaged. The images were then convolved to the lowest resolution given by the 325 MHz GMRT observations ($9.1'' \times 6.5''$). The spectral index map for the area around A (indicated by the dashed square in Fig. 2a) is shown in the Supplementary Information. We also computed a higher signal-to-noise spectral index map, including the 0.61 and 1.5 GHz observations. As before, the 0.61 and 1.5 GHz observations were imaged with uniform weighting and inner u - v -range cuts. To compute the spectral index, we fitted power-law

spectra to the four data points, ignoring any possible curvature. Pixels with values below $4\sigma_{\text{rms}}$ were ‘blanked’. The use of four frequencies decreases the noise on the derived spectral indices compared with only using the 0.325 and 3.0 GHz images. The spectral index map and corresponding uncertainties, under the assumption that the spectra can be described by power laws, are shown in the Supplementary Information (a cutout around source A is shown in Fig. 3b).

The S-band polarization image is shown in Fig. 3c and has a resolution of $10'' \times 8''$. No vectors were plotted for pixels where the signal-to-noise ratio (S/R) of the polarized intensity was <4 . Given the low galactic Faraday rotation measure of $\sim -7 \text{ rad m}^{-2}$, we did not correct the polarization angles for Faraday rotation³⁶. The high-resolution S-band continuum map, showing the radio core associated with the AGN of source A, is provided in the Supplementary Information.

We computed the probability of a chance projection of the tailed radio galaxy with the relic attached to it. This was done by taking the ratio of the area covered by the relic and the area covered by the cluster, with the cluster area given by $\pi \times R_{500}^2$, and $R_{500} \approx 1.4 \text{ Mpc}$. The resulting probability was 0.2%. Taking a conservative approach: considering that the cluster contains two disturbed radio galaxies, the probability of a chance projection increases to 0.4%.

The cluster contains at least two more radio galaxies (B and C, see Fig. 2) to the south and southwest of the one described above. One of the radio galaxies (source B) is embedded within the relic emission. Source C is a distorted FR-I³⁷ source. The spectral index map and the 325 MHz image (Supplementary Information and Fig. 2) reveal a hint of a connection between the southern lobe/tail of source C and the southernmost part of the relic. The spectral index steepens along the lobes of source C, as expected due to synchrotron and inverse Compton losses. Given that the relic emission around sources B and C is located further to the south than the relic near source A, it seems unlikely that the same shock is responsible for reviving the fossil plasma in all these regions. This would suggest that the ICM in the extreme southern outskirts of the cluster is disturbed by other shocks. Our Chandra observations do show the presence of additional substructure in the general area around sources B and C. However, given the low count rates, it is not possible to extract detailed information on the thermal properties of the ICM in this region.

Chandra observations and data reduction. The cluster was observed eight times with the Advanced CCD Imaging Spectrometer I-array (ACIS-I) on the Chandra X-ray Observatory between 2012 and 2015. This resulted in a total exposure time of 211 ks. The data were reduced using the chav software package (Alexey Vikhlinin, Smithsonian Astrophysical Observatory), following the processing described in³⁸ and applying the CALDB 4.6.7 calibration files. This processing includes filtering of bad events by checking for periods of high background, corrections for the time dependence of the charge transfer inefficiency and gain, removal of readout artifacts, background subtraction, and exposure correction. For the background subtraction, we used standard blank sky background files. The images of the separate exposures were then combined into a single image, binning with a factor of 4; that is, $2''$ per pixel.

Surface brightness profile fitting. We fitted the X-ray surface brightness profile with an updated version of Proffit^{39,40}. We modeled the ICM density profile ($n(r)$) using an underlying broken power-law density model:

$$n(r) = \begin{cases} C n_0 \left(\frac{r}{r_{\text{edge}}} \right)^{a_2} & , \quad r < r_{\text{edge}} \\ n_0 \left(\frac{r}{r_{\text{edge}}} \right)^{a_1} & , \quad r > r_{\text{edge}} \end{cases} \quad (1)$$

The subscripts 1 and 2 refer to the up- and down-stream regions, respectively. The parameter r_{edge} denotes the location of the jump, n_0 is the normalization constant, C is the shock compression factor, and a_1 and a_2 are the slopes of the power laws. This density model was then projected along the line of sight to obtain an X-ray surface brightness profile, assuming prolate spheroidal geometry within the sector. The emissivity was taken to be proportional to the density squared.

In the case of a shock, the compression factor can be related to the Mach number of the shock

$$M = \left[\frac{2C}{\gamma + 1 - C(\gamma - 1)} \right]^{1/2} \quad (2)$$

where γ is the adiabatic index of the gas. We assume $\gamma = 5/3$ for the thermal plasma.

We fitted the surface brightness profile in an elliptical sector that crosses the radio relic (see the Supplementary Information), using the model given in equation (1). The opening angles (210° – 250°) were chosen after visual inspection of the Chandra image (see the Supplementary Information), which suggests a surface brightness edge at the relic location and extending $\sim 10^\circ$ further to the west. For the radial binning of photons, we required a S/R of five per bin. We excluded the regions affected by point sources during the fitting. The observed profile and

the best fitting model are shown in Fig. 4. We found a break in the X-ray surface brightness profile at the location of the radio relic. The resulting compression factor (location indicated in Fig. 3b) was small, $C=1.31^{+0.10}_{-0.09}$ ($M=1.2$); the upper 90% confidence limit was 1.56, indicating a low Mach number ($M < 1.4$), and the lower limit was 1.16.

We also extracted a profile in a spherical sector (see the Supplementary Information). The resulting fitted compression factor was slightly lower, at ~ 1.2 , but consistent with our other results. In addition, we checked whether the results changed for a smaller opening angle (210° – 240°), corresponding to the relic's visible extent in the 610 and 325 MHz images. This did not result in significant changes for the values of the compression factor or discontinuity location. We also slightly varied the placement of the sector, and again obtained consistent results. Therefore, we conclude that the presence of a discontinuity does not depend on the precise sector placement and shape. For comparison, in the Supplementary Information we show a model where the compression factor increases to 2.3 ($M=2.0$) in the elliptical sector; however, this model is not a good match for the data.

A small 'bump' is visible in the X-ray surface brightness profile at a radial distance of $4.5' - 5.0'$ (Fig. 4); however, its nature is unclear. Ignoring the bump increases the best-fitting compression factor, with its 90% confidence upper limit rising to 2.0 ($M < 1.7$).

From the X-ray surface brightness profile, we conclude that there is evidence for a deviation from hydrostatic equilibrium as expected if a shock were present. The location of the discontinuity coincides with the location of the relic, and is consistent with the location determined by visual inspection of the Chandra image. The modeling suggests that the underlying jump in density must be rather low ($C < 2.0$, $M < 1.7$). Some caution is required in interpreting the derived Mach number and upper limits, since it depends on the assumptions made in the modeling. Given the extra substructure in this region, as seen in the Chandra image, some of the assumptions might be incorrect. Unknown projection effects and shock geometry typically result in underestimation of the Mach number and our derived values should therefore be considered as lower limits.

Another way to constrain the Mach number, and rule out the presence of a cold front, is to determine the temperatures on both sides of the discontinuity (in a small enough region as not to be affected by other cluster substructure). An advantage of this method is that temperature measurements are less affected by the unknown geometry. However, the count rate in the region south of the discontinuity is very low, and therefore we were not able to obtain useful constraints on the pre-shock X-ray gas temperature.

SOAR spectroscopy and data reduction. The optical spectrum of the AGN host galaxy that 'fuels' the relic (RA 08 h 42 min 13.73 s; dec. $-17^\circ 31' 12.1''$) was acquired using the Goodman Spectrograph on the Southern Astrophysical Research Telescope (SOAR) telescope. The observations were conducted on 19 November 2015, as part of programme SO2015B-020. The basic setup included a 600 line mm^{-1} grating (blue setting) and a $1.03''$ slit. The wavelength range of the observed spectrum was 3,500–5,500 Å, with a resolving power of $R \sim 1,500$ and a S/N of $\sim 10 \text{ pixel}^{-1}$ at 4,500 Å. Calibration frames included Cu and HgAr arc-lamp exposures, quartz-lamp flat-fields and bias frames. The data reduction, including spectral extraction and wavelength calibration, were performed using standard Image Reduction and Analysis Facility (IRAF) routines (<http://iraf.noao.edu>).

A SOAR optical spectrum of the AGN host galaxy is shown in the Supplementary Information. From the spectrum we determined a redshift of $z=0.164 \pm 0.001$, consistent with the galaxy being a cluster member.

Subaru and Keck observations. We carried out deep imaging observations of the Abell 3411–3412 system with the Subaru SuprimeCam⁴¹ on 24 February 2014, using g-, r- and i-band filters with integrations of 720 s, 2,880 s and 720 s, respectively (principal investigator, D. Wittman). We took four exposures for g and i, and eight exposures for r. We rotated the field between each exposure (30° for g and i, and 15° for r) to distribute the bleeding trails and diffraction spikes from bright stars azimuthally and later removed them using median-stacking exposures. This scheme enabled us to maximize the number of detected galaxies, especially considering the number of stars at A3411–3412's low galactic latitude ($\sim 15^\circ$). The average seeing for the images was $\sim 0.85''$. The details of the Subaru data reduction are similar to those reported previously⁴².

The primary objective for the spectroscopic survey was to maximize the number of cluster-member spectroscopic redshifts. Since the SuprimeCam imaging was unavailable at the time of the spectroscopic survey planning, we took g- and i-band images with the Isaac Newton Telescope Wide Field Camera (INT/WFC) on 31 October 2013, to determine the approximate red sequence of the cluster and preferentially select those galaxies followed by potential blue cloud galaxies. These INT/WFC data were reduced using our in-house PYTHON-based pipeline^{43,44}. Briefly, the sky flats for each filter were median-combined to obtain a 'master flat'. A 'master bias' was obtained by median-combining biases. The individual exposures were then bias-subtracted and sky-flattened. Astrometric solutions were obtained using SCAMP⁴⁵, and images were zero-point calibrated with the fourth United States Naval Observatory CCD Astrograph Catalog

(UCAC4)⁴⁶, before being stacked/combined using SWARP⁴⁷. The difficulty of star–galaxy separation is compounded by the $1.5''$ – $2.0''$ seeing of the INT/WFC imaging, which results in many blended pairs of stars passing morphological cuts designed to eliminate point sources.

We observed the Abell 3411–3412 system with the DEIMOS⁴⁸ instrument on the Keck II 10-m telescope on 3 and 4 December 2013. Observations were captured using $1''$ wide slits and a 1,200 line mm^{-1} grating, resulting in a pixel scale of $0.33 \text{ Å pixel}^{-1}$ and a resolution of $\sim 1 \text{ Å}$ (50 km s^{-1}). The grating was tilted to a central wavelength of 6,650 Å, resulting in a typical wavelength coverage of 5,350 Å to 7,950 Å, which encompasses the spectral features H β , [O III] 4960 and 5008, Mg I (b), Fe I, Na I (D), [O I], H α , and the [N II] doublet for galaxies near the cluster redshift. The actual wavelength coverage may be shifted by approximately $\pm 410 \text{ Å}$ depending on where the slit is located along the width of the slitmask. We observed a total of four slit masks with approximately 120 slits per mask. For each mask we took three 900 s exposures. A detailed account of the data reduction procedure is given elsewhere^{44,49}.

We obtained 484 spectra with DEIMOS. Of these, we obtained reliable redshifts for 447 objects (92%), leaving 37 spectra that were too noisy, had ambiguous redshift solutions (for example, those with a single emission line) or failed to reduce properly. Of the 447 reliable redshifts, 221 (49%) corresponded to stars, indicating the difficulty of star–galaxy discrimination with low-resolution imaging at low Galactic latitude. Adopting a previously described quality rating system⁵⁰, in which only galaxies with secure redshifts ($Q > 3$) are considered to be of high quality, the removal of the stars results in 226 high-quality DEIMOS galaxy spectra. Of these, 174 (77%) fall within $0.148 \leq z \leq 0.176$ (see the Supplementary Information), which is $z_{\text{cluster}} \pm 3\sigma$, where $z_{\text{cluster}} = 0.162$ and σ is the approximate velocity dispersion ($1,000 \text{ km s}^{-1}$). The remaining 52 high-quality spectra consist of one foreground and 51 background galaxies, respectively comprising 0.4% and 23% of these spectra. The subcluster identification and the dynamical modeling are described in the Supplementary Information.

Data availability. The data that support the plots within this paper and other findings of this study are available from the corresponding author upon reasonable request.

Received 28 July 2016; accepted 8 November 2016;
published 4 January 2017

References

1. Feretti, L., Giovannini, G., Govoni, F. & Murgia, M. Clusters of galaxies: observational properties of the diffuse radio emission. *Astron. Astrophys. Rev.* **20**, 54 (2012).
2. Brunetti, G. & Jones, T. W. Cosmic rays in galaxy clusters and their nonthermal emission. *Int. J. Mod. Phys. D* **23**, 1430007–98 (2014).
3. Ensslin, T. A., Biermann, P. L., Klein, U. & Kohle, S. Cluster radio relics as a tracer of shock waves of the large-scale structure formation. *Astron. Astrophys.* **332**, 395–409 (1998).
4. Ryu, D., Kang, H., Hallman, E. & Jones, T. W. Cosmological shock waves and their role in the large-scale structure of the Universe. *Astrophys. J.* **593**, 599–610 (2003).
5. Kang, H. & Ryu, D. Cosmic ray spectrum from diffusive shock acceleration. *Astrophys. Space Sci.* **336**, 263–268 (2011).
6. Macario, G. *et al.* A shock front in the merging galaxy cluster A754: X-ray and radio observations. *Astrophys. J.* **728**, 82 (2011).
7. Shimwell, T. W. *et al.* Another shock for the Bullet cluster, and the source of seed electrons for radio relics. *Mon. Not. R. Astron. Soc.* **449**, 1486–1494 (2015).
8. Kang, H., Ryu, D. & Jones, T. W. Diffusive shock acceleration simulations of radio relics. *Astrophys. J.* **756**, 97 (2012).
9. Pinzke, A., Oh, S. P. & Pfrommer, C. Giant radio relics in galaxy clusters: reacceleration of fossil relativistic electrons? *Mon. Not. R. Astron. Soc.* **435**, 1061–1082 (2013).
10. Vazza, F. & Brüggen, M. Do radio relics challenge diffusive shock acceleration? *Mon. Not. R. Astron. Soc.* **437**, 2291–2296 (2014).
11. Itahana, M. *et al.* Suzaku observations of the galaxy cluster 1RXS J0603.3+4214: implications of particle acceleration processes in the "Toothbrush" radio relic. *Publ. Astron. Soc. Jpn.* **67**, 113 (2015).
12. van Weeren, R. J. LOFAR, VLA, and Chandra observations of the Toothbrush galaxy cluster. *Astrophys. J.* **818**, 204 (2016).
13. Blandford, R. & Eichler, D. Particle acceleration at astrophysical shocks: a theory of cosmic ray origin. *Phys. Rep.* **154**, 1–75 (1987).
14. Russell, H. R. *et al.* A merger mystery: no extended radio emission in the merging cluster Abell 2146. *Mon. Not. R. Astron. Soc.* **417**, 1–5 (2011).
15. Guo, X., Sironi, L. & Narayan, R. Non-thermal Electron acceleration in low mach number collisionless shocks. II. Firehose-mediated Fermi acceleration and its dependence on pre-shock conditions. *Astrophys. J.* **797**, 47 (2014).
16. Botteon, A., Gastaldello, F., Brunetti, G. & Dallacasa, D. A shock at the radio relic position in Abell 115. *Mon. Not. R. Astron. Soc.* **460**, 84–88 (2016).

17. Eckert, D. *et al.* A shock front at the radio relic of Abell 2744. *Mon. Not. R. Astron. Soc.* **461**, 1302–1307 (2016).
18. Markevitch, M., Govoni, F., Brunetti, G. & Jerius, D. Bow shock and radio halo in the merging cluster A520. *Astrophys. J.* **627**, 733–738 (2005).
19. Kang, H. & Ryu, D. Curved radio spectra of weak cluster shocks. *Astrophys. J.* **809**, 186 (2015).
20. Bonafede, A. *et al.* Evidence for particle re-acceleration in the radio relic in the galaxy cluster PLCKG287.0+32.9. *Astrophys. J.* **785**, 1 (2014).
21. Giovannini, G., Feretti, L. & Stanghellini, C. The Coma cluster radio source 1253+275, revisited. *Astron. Astrophys.* **252**, 528–537 (1991).
22. Bagchi, J. *et al.* Discovery of the first giant double radio relic in a galaxy cluster found in the Planck Sunyaev-Zeldovich Cluster Survey: PLCK G287.0+32.9. *Astrophys. J.* **736**, 8 (2011).
23. Enßlin, T. A. & Gopal-Krishna, Reviving fossil radio plasma in clusters of galaxies by adiabatic compression in environmental shock waves. *Astron. Astrophys.* **366**, 26–34 (2001).
24. Enßlin, T. A. & Brüggen, M. On the formation of cluster radio relics. *Mon. Not. R. Astron. Soc.* **331**, 1011–1019 (2002).
25. van Weeren, R. J. *et al.* Complex diffuse radio emission in the merging Planck ESZ Cluster A3411. *Astrophys. J.* **769**, 101 (2013).
26. Giovannini, G. *et al.* The nature of the giant diffuse non-thermal source in the A3411-A3412 complex. *Mon. Not. R. Astron. Soc.* **435**, 518–523 (2013).
27. van Weeren, R. J., Röttgering, H. J. A., Brüggen, M. & Hoeft, M. Particle acceleration on megaparsec scales in a merging galaxy cluster. *Science* **330**, 347 (2010).
28. Fujita, Y., Takizawa, M., Yamazaki, R., Akamatsu, H. & Ohno, H. Turbulent cosmic-ray reacceleration at radio relics and halos in clusters of galaxies. *Astrophys. J.* **815**, 116 (2015).
29. Vazza, F., Eckert, D., Brüggen, M. & Huber, B. Electron and proton acceleration efficiency by merger shocks in galaxy clusters. *Astrophys. J.* **451**, 2198–2211 (2015).
30. Stockem, A., Fiuza, F., Bret, A., Fonseca, R. A. & Silva, L. O. Exploring the nature of collisionless shocks under laboratory conditions. *Sci. Rep.* **4**, 3934 (2014).
31. McMullin, J. P., Waters, B., Schiebel, D., Young, W. & Golap, K. in *Astronomical Data Analysis Software and Systems XVI* (eds Shaw, R. A., Hill, F. & Bel, D. J.) 127 (Astron. Soc. Pacif. Conf. Ser. Vol. 376, 2007).
32. Cornwell, T. J., Golap, K. & Bhatnagar, S. The noncoplanar baselines effect in radio interferometry: the W-projection algorithm. *IEEE J. Sel. Top. Signal Process.* **2**, 647–657 (2008).
33. Cornwell, T. J., Golap, K. & Bhatnagar, S. W in *Astronomical Data Analysis Software and Systems XIV* (eds Shopbel, P. L., Britton, M. & Ebert, R.) 86 (Astron. Soc. Pacif. Conf. Ser. Vol. 376, 2005).
34. van Weeren, R. J. *et al.* The discovery of lensed radio and X-Ray sources behind the frontier fields cluster MACS J0717.5+3745 with the JVLA and Chandra. *Astrophys. J.* **817**, 98 (2016).
35. Offringa, A. R. *et al.* Post-correlation radio frequency interference classification methods. *Mon. Not. R. Astron. Soc.* **405**, 155–167 (2010).
36. Taylor, A. R., Stil, J. M. & Sunstrum, C. A Rotation measure image of the sky. *Astrophys. J.* **702**, 1230–1236 (2009).
37. Fanaroff, B. L. & Riley, J. M. The morphology of extragalactic radio sources of high and low luminosity. *Mon. Not. R. Astron. Soc.* **167**, 31–36 (1974).
38. Vikhlinin, A. *et al.* Chandra temperature profiles for a sample of nearby relaxed galaxy clusters. *Astrophys. J.* **628**, 655–672 (2005).
39. Eckert, D., Molendi, S. & Paltani, S. The cool-core bias in X-ray galaxy cluster samples. I: Method and application to HIFLUGCS. *Astron. Astrophys.* **526**, 79 (2011).
40. Ogrean, G. A. *et al.* Challenges to our understanding of radio relics: X-ray observations of the Toothbrush cluster. *Mon. Not. R. Astron. Soc.* **433**, 812–824 (2013).
41. Miyazaki, S. *et al.* Subaru Prime Focus Camera — Suprime-Cam. *Publ. Astron. Soc. Jpn.* **54**, 833–853 (2002).
42. Jee, M. J. *et al.* MC²: Constraining the dark matter distribution of the violent merging galaxy cluster CIZA J2242.8+5301 by piercing through the milky Way. *Astrophys. J.* **802**, 46 (2015).
43. Stroe, A. *et al.* The role of cluster mergers and travelling shocks in shaping the Ha luminosity function at $z \sim 0.2$: ‘sausage’ and ‘toothbrush’ clusters. *Mon. Not. R. Astron. Soc.* **438**, 1377–1390 (2014).
44. Sobral, D. *et al.* MC²: boosted AGN and star formation activity in CIZA J2242.8+5301, a massive post-merger cluster at $z=0.19$. *Mon. Not. R. Astron. Soc.* **450**, 630–645 (2015).
45. Bertin, E. in *Astronomical Data Analysis Software and Systems* (eds Gabriel, C., Arviset, C., Ponz, D. & Enrique, S.) 112 (Astron. Soc. Pacif. Conf. Ser. Vol. 351, 2006).
46. Zacharias, N. *et al.* The Fourth US Naval Observatory CCD Astrograph Catalog (UCAC4) *Astron. J.* **145**, 44 (2013).
47. Bertin, E. *et al.* in *Astronomical Data Analysis Software and Systems XI* (eds Bohlender, D. A., Durand, D. & Handley, T. H.) 228 (Astron. Soc. Pacif. Conf. Ser. Vol. 281, 2002).
48. Faber, S. M. *et al.* in *Proc. SPIE - International Society for Optical Engineering* (eds Iye, M. & Moorwood, A. F. M.) Vol. 4841, 1657–1669 (International Society for Optics and Photonics, 2003).
49. Dawson, W. A. *et al.* MC²: galaxy imaging and redshift analysis of the merging cluster CIZA J2242.8+5301. *Astrophys. J.* **805**, 143 (2015).
50. Newman, J. A. *et al.* The DEEP2 Galaxy Redshift Survey: design, observations, data reduction, and redshifts. *Astrophys. J. Suppl. Ser.* **208**, 5 (2013).

Acknowledgements

Support for this work was provided by the National Aeronautics and Space Administration through Chandra Award Numbers GO3-14131X and GO5-16133X issued by the Chandra X-ray Observatory Center, which is operated by the Smithsonian Astrophysical Observatory for and on behalf of the National Aeronautics Space Administration under Contract NAS8-03060. We thank the staff of the Giant Metrewave Radio Telescope (GMRT) who have made these observations possible. The GMRT is run by the National Centre for Radio Astrophysics of the Tata Institute of Fundamental Research. The National Radio Astronomy Observatory is a facility of the National Science Foundation operated under cooperative agreement by Associated Universities, Inc. Based on observations obtained at the Southern Astrophysical Research (SOAR) telescope, which is a joint project of the Ministério da Ciência, Tecnologia, e Inovação (MCTI) da República Federativa do Brasil, the US National Optical Astronomy Observatory (NOAO), the University of North Carolina at Chapel Hill (UNC), and Michigan State University (MSU). Based on data collected at Subaru Telescope, which is operated by the National Astronomical Observatory of Japan. Part of this work was performed under the auspices of the US DOE by LLNL under Contract DE-AC52-07NA27344. Some of the data presented herein were obtained at the W.M. Keck Observatory, which is operated as a scientific partnership between the California Institute of Technology, the University of California and the National Aeronautics and Space Administration. The Observatory was made possible by the generous financial support of the W.M. Keck Foundation. The Isaac Newton Telescope is operated on the island of La Palma by the Isaac Newton Group in the Spanish Observatorio del Roque de los Muchachos of the Instituto de Astrofísica de Canarias. R.J.W. was supported by a Clay Fellowship awarded by the Harvard-Smithsonian Center for Astrophysics. V.M.P. acknowledges support for this work from grant PHY 14-30152; Physics Frontier Center/JINA Center for the Evolution of the Elements (JINA-CEE), awarded by the US National Science Foundation. D.R. was supported by the National Research Foundation of Korea through Grant 2016R1A5A1013277. H.K. was supported by the National Research Foundation of Korea through Grant 2014R1A1A2057940. R.M.S. acknowledges CAPES (PROEX), CNPq, PRPG/USP, FAPESP and INCT-A funding. M.J.J. acknowledges support from KASI and NRF of Korea to CGER. D.S. acknowledges financial support from the Netherlands Organisation for Scientific research (NWO) through a Veni fellowship. G.A.O. is supported by NASA through Hubble Fellowship Grant HST-HF2-51345.001-A, awarded by the Space Telescope Science Institute, which is operated by the Association of Universities for Research in Astronomy, Inc., for NASA, under Contract NAS5-26555.

Author contributions

R.J.W. coordinated the research, wrote the manuscript, reduced the VLA data, and led the Chandra observing proposal. F.A.S., K.F. and G.A.O. performed the Chandra data reduction and worked on the X-ray surface brightness profile fitting. H.K. and D.R. carried out the re-acceleration modeling. M.B., W.R.F. and C.J. helped with the interpretation of the radio and X-ray results and provided extensive feedback on the manuscript. C.J. led the GMRT observing proposal. D.V.L. obtained the GMRT observations and carried out the GMRT data reduction. V.M.P. and R.M.A. obtained the SOAR observations and performed the corresponding data reduction. D.S. and A.S. obtained the INT observations and reduced the data. W.A.D. carried out the dynamical modeling of the merger event. W.A.D., N.G. and M.J.J. obtained the Keck and Subaru observations and reduced the data. D.W. helped with the interpretation of the dynamical modeling and led the Keck and Subaru observing proposals. R.P.K. assisted with the writing of the Chandra observing proposal.

Additional information

Supplementary information is available for this paper.

Reprints and permissions information is available at www.nature.com/reprints.

Correspondence and requests for materials should be addressed to R.J.W.

How to cite this article: van Weeren, R. J. *et al.* The case for electron re-acceleration at galaxy cluster shocks. *Nat. Astron.* **1**, 0005 (2017).

Competing interests

The authors declare no competing financial interests.